





**Sandia National Laboratories**

Operated for the United States Department of Energy  
by National Technology and Engineering Solutions  
of Sandia, LLC.

Albuquerque, New Mexico 87185  
Livermore, California 94550

*date:* August 8, 2025

*to:* Distribution

*from:* Alvin Chen  (1558), Michael R. Buche  (1558)

*subject:* Efforts to stabilize composite localization elements

## Abstract

Localization finite elements seek to provide a robust framework for modeling ductile failure. They utilize the same constitutive model as the bulk material through the introduction of a length scale in a specialized deformation gradient that regularizes displacement discontinuity. Similar to many other elements, localization elements exhibit locking and associated pressure oscillations under incompressible plastic flow, which is a critical issue when attempting to model pressure-driven damage evolution. These issues can be drastically improved through what are essentially reduced integration techniques for the Jacobian and pressure, but there seem to be pressure-related instabilities that persist and are specific to localization elements. This memo summarizes recent efforts to mitigate and understand this problem, mostly for the 12-node composite wedge localization element in particular. At this point, it remains unclear whether the pressure fields within any localization element can be sufficiently stabilized in order to properly model failures that include softening or fracture.

## Background

The Helmholtz free energy  $A$  of a body  $\Omega$  containing a localization surface is postulated as

$$\int_{\Omega} A(\mathbf{F}, \mathbf{Z}) dV = \sum_{\pm} \int_{\Omega_{\pm}} A(\mathbf{F}, \mathbf{Z}) dV + \int_{\Gamma} A(\mathbf{F}, \mathbf{Z}) h dS, \quad (1)$$

where  $\mathbf{F}$  is the deformation gradient,  $\mathbf{Z}$  are the internal state variables,  $\Omega_{\pm}$  is the body above or below the localization surface  $\Gamma$ , in the reference configuration, and  $h$  is a length scale [1]. The localization surface is primarily described by the discontinuous displacement jump  $[\![\boldsymbol{\varphi}]\!]$  in the current configuration, as shown in Fig. 1. The deformation gradient is postulated as

$$\mathbf{F} = \mathbf{F}^{\parallel} \mathbf{F}^{\perp}, \quad (2)$$

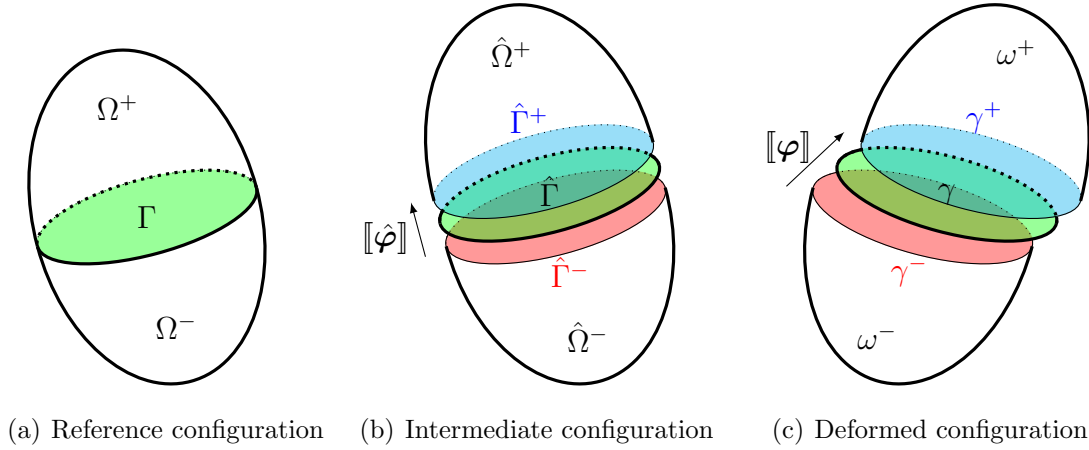


**Figure 1.** Schematic of a body undergoing an internal localized surface deformation.

where  $\mathbf{F}^{\parallel}$  is the membrane deformation and  $\mathbf{F}^{\perp}$  is the transverse deformation, and the multiplicative decomposition is motivated by that observed in single-crystal plasticity [1]. The membrane deformation is given by that for an embedded surface,

$$\mathbf{F}^{\parallel} = \mathbf{g}_{\mu} \otimes \hat{\mathbf{G}}^{\mu} + \mathbf{n} \otimes \hat{\mathbf{N}}, \quad (3)$$

which is formulated in terms of the surface tangent basis, dual basis, normal vectors in the deformed and intermediate configurations. The transverse deformation is given by

$$\mathbf{F}^{\perp} = \mathbf{I} + \frac{[[\hat{\varphi}]]}{h} \otimes \mathbf{N}, \quad (4)$$

where  $[[\hat{\varphi}]]$  is the displacement jump in the intermediate configuration, also shown in Fig. 2. Note that the intermediate configuration is necessary to ensure that the deformation gradient in Eq. (2) is objective, as opposed to Yang et al. [1]. Further, Eq. (2) can now be rewritten as an additive decomposition which does not involve the intermediate configuration,

$$\mathbf{F} = \mathbf{g}_{\mu} \otimes \mathbf{G}^{\mu} + \mathbf{n} \otimes \mathbf{N} + \frac{[[\varphi]]}{h} \otimes \mathbf{N}, \quad (5)$$

which leverages the relation  $[[\varphi]] = \mathbf{F}^{\parallel}[[\hat{\varphi}]]$  as well as the fact that  $\mathbf{G}^{\mu} = \hat{\mathbf{G}}^{\mu}$  and  $\mathbf{N} = \hat{\mathbf{N}}$ . Briefly, the introduction of a separate length scale  $t$  in Eq. (1) has been considered. This would weight a separate energetic contribution from the membrane deformation, while  $h$  weights another separate contribution from the transverse deformation and regularizes the displacement jump. Unfortunately, this separation was incompatible with clearly defining an energy such as Eq. (1) and created numerical difficulties, so it was not pursued further.



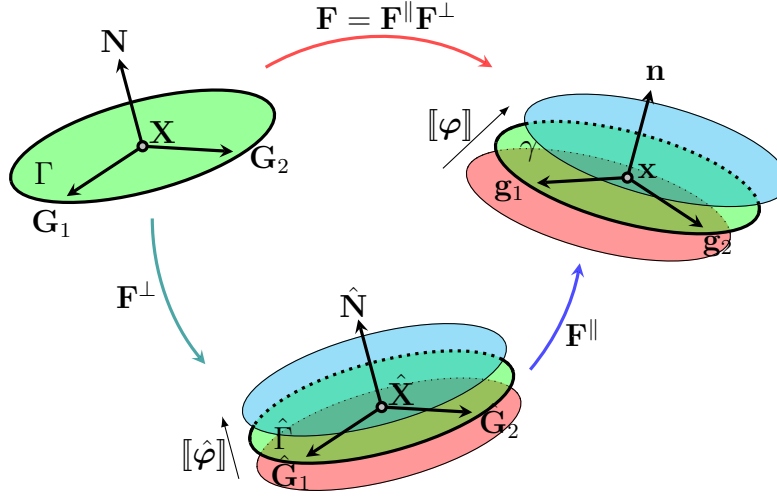


**Figure 2.** Kinematics of the deformation corresponding to a localization surface.

The 12-node composite wedge localization finite element was developed to be compatible with the 10-node composite tetrahedral finite element from Foulk III et al. [2], so it used a similar functional representation of the energy. For the localization surfaces only, this is

$$\Pi[\varphi, \bar{\mathbf{F}}, \bar{\mathbf{P}}] = \int_{\Gamma} A(\bar{\mathbf{F}}, \mathbf{Z}) h dS + \int_{\Gamma} \bar{\mathbf{P}} : (\mathbf{F} - \bar{\mathbf{F}}) h dS, \quad (6)$$

where  $\bar{\mathbf{F}}$  is a separate deformation gradient that is constrained to equal  $\mathbf{F}$  through the Lagrange multiplier  $\bar{\mathbf{P}}$ . Discretizing via nodal coordinates  $\mathbf{x}_a$  and basis functions  $N_a$ , the mid-surface is  $\tilde{\mathbf{x}}_a = \frac{1}{2}(\mathbf{x}_a^+ + \mathbf{x}_a^-)$  and the displacement jump is  $[[\mathbf{x}_a]] = \mathbf{x}_a^+ - \mathbf{x}_a^-$ , as in Fig. 3. The deformation gradient in Eq. (5) can then be written in terms of gradient operators as

$$\mathbf{F} = \mathcal{B}_a^g \tilde{\mathbf{x}}_a + \mathcal{B}_a^n(\tilde{\mathbf{x}}_a) + \mathcal{B}_a^\perp [[\mathbf{x}_a]] := \mathcal{B}_a^\parallel(\tilde{\mathbf{x}}_a) + \mathcal{B}_a^\perp [[\mathbf{x}_a]], \quad (7)$$

where unfortunately,  $\mathcal{B}_a^\parallel$  still depends on  $\mathbf{x}_a$  due to the nonlinear dependence of  $\mathbf{n}$  on  $\mathbf{x}_a$ , i.e.,  $\mathbf{n} = \frac{\mathbf{g}_1 \times \mathbf{g}_2}{|\mathbf{g}_1 \times \mathbf{g}_2|}$  where  $\mathbf{g}_\mu = \frac{\partial N_a}{\partial \xi^\mu} \mathbf{x}_a$ . Conversely  $\mathcal{B}_a^\perp = \frac{1}{h} N_a \mathbf{N}$  is quite simple, so the nodal forces

$$\mathbf{R}_a^\pm = \frac{1}{2} \int_{\Gamma} \bar{\mathbf{P}} : \frac{\partial \mathcal{B}_a^\parallel}{\partial \tilde{\mathbf{x}}_a} h dS \pm \int_{\Gamma} \bar{\mathbf{P}} \mathbf{N} N_a dS, \quad (8)$$

produce a term that resembles nodal forces for cohesive surface elements [3] via traction  $\bar{\mathbf{P}} \mathbf{N}$ . However, the two are still quite different since the traction for cohesive surface elements depends on displacements and specialized cohesive zone models, while the traction here depends on a specialized deformation gradient and the same constitutive model as the bulk.

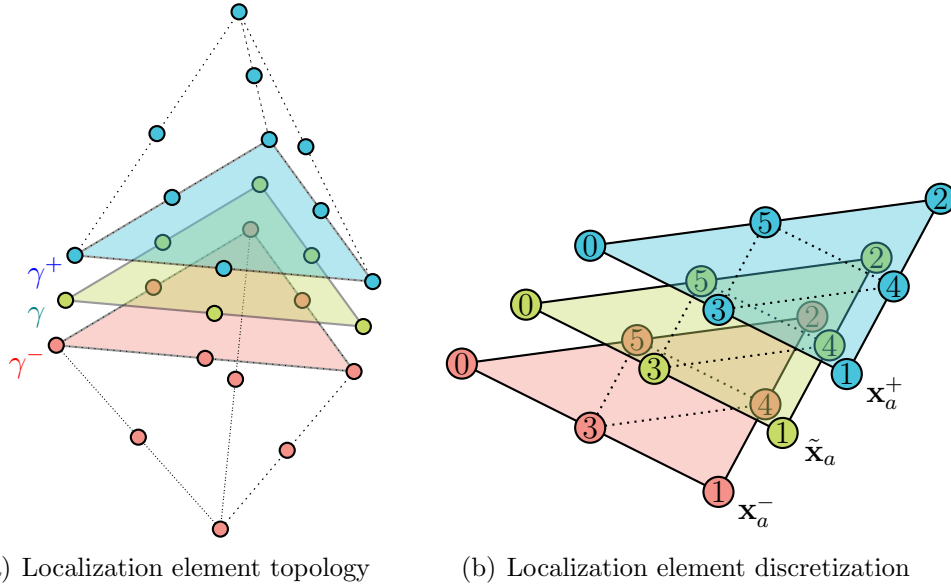


**Figure 3.** Mesh topology and discretization of a composite localization element.

Eq. (8) is often rewritten in terms of the projected gradient operators  $\bar{\mathcal{B}}_a$  and the stress  $\mathbf{P}$  evaluated at the projected deformation gradient  $\bar{\mathbf{F}}$ , where the projection refers to quantities at each linear subelement being projected to a linear parent element [2]. Much of  $\bar{\mathcal{B}}_a$  can be pre-computed, but part of it cannot due to the dependence on  $\mathbf{n}$  described earlier [4]. The Jacobian is also projected to the four integration points for optimal integration weights [2]. These calculations are considerable but are not detailed here. The composite localization element was implemented within Sierra/Solid Mechanics [5], and they were typically inserted into an existing mesh similarly to cohesive surface elements using Exomerge [6].

For the examples in this memo, we use, unless specified, the model problem of a notched bar under tension. The bar has a height of 60 mm, the ends have radius 15 mm, and the middle notch has a minimum radius of 5 mm. The material has Young's modulus  $E = 1.17 \times 10^5$  MPa, and Poisson's ratio  $\nu = 0.33$ . The material is governed by a J2-plasticity model with linear hardening, a yield stress of  $5.64 \times 10^2$  MPa and a hardening modulus of  $1.07 \times 10^3$  MPa. The bar is meshed using 10-node composite tetrahedrons and a single layer of wedge localization elements through the mid-section (see Fig. 4).

### Lower-order projection and stabilization

For problems in plasticity and with nearly-incompressible materials, it is found that using the formulation (6) results in volumetric locking. In order to alleviate some of the locking, we follow the approach in [2] and introduce a lower-order projection for the pressure and the

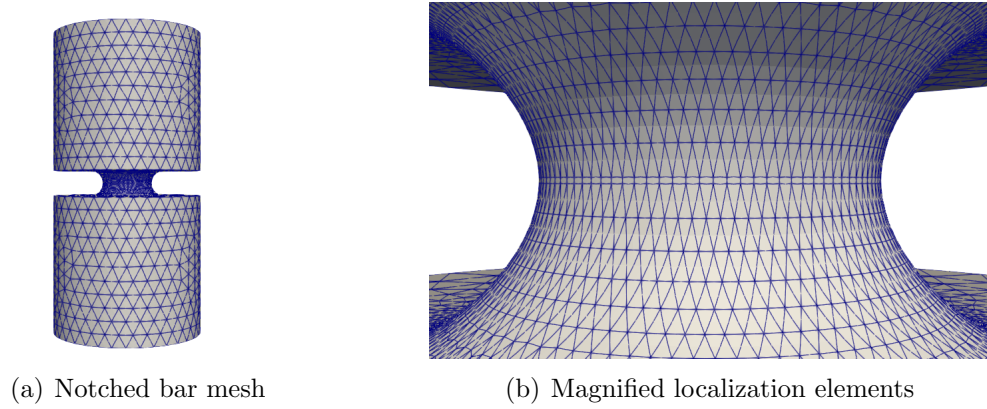


**Figure 4.** Representative example of a mesh used for the notched tension problem and a magnified plot showing the corresponding localization elements (deformed).

Jacobian in a five-field functional:

$$\begin{aligned} \Pi^*[\boldsymbol{\varphi}, \bar{\mathbf{F}}, \bar{\mathbf{P}}, \bar{p}^*, \bar{J}^*] := & \int_{\Gamma} A \left( \left( \frac{\bar{J}^*}{\bar{J}} \right)^{1/3} \bar{\mathbf{F}}, \mathbf{Z} \right) h dS \\ & + \int_{\Gamma} \bar{\mathbf{P}} : (\mathbf{F} - \bar{\mathbf{F}}) h dS + \int_{\Gamma} \bar{p}^* (\bar{J} - \bar{J}^*) h dS, \end{aligned} \quad (9)$$

where  $\bar{J} = \det \bar{\mathbf{F}}$ ,  $\bar{p}^*$  is the projected pressure, and  $\bar{J}^*$  is the projected Jacobian. After taking the variation of  $\Pi^*[\cdot]$  and requiring it to be stationary, we obtain the weak equilibrium equations and projection relations

$$\int_{\Gamma} (\bar{\mathbf{P}} : \text{Grad}(\delta \boldsymbol{\varphi})) h dS = 0, \quad (10a)$$

$$\int_{\Gamma} \left[ \left( \frac{\bar{J}^*}{\bar{J}} \right)^{1/3} \left( \tilde{\mathbf{P}} - \frac{1}{3} \text{tr}(\tilde{\mathbf{P}} \tilde{\mathbf{F}}^T) \tilde{\mathbf{F}}^{-T} + \bar{J} \bar{p}^* \tilde{\mathbf{F}}^{-T} \right) - \bar{\mathbf{P}} \right] : \delta \bar{\mathbf{F}} h dS = 0, \quad (10b)$$

$$\int_{\Gamma} \left( \frac{1}{3\bar{J}} \text{tr}(\tilde{\mathbf{P}} \tilde{\mathbf{F}}^T) - \bar{p}^* \right) \delta \bar{J}^* h dS = 0, \quad (10c)$$

$$\int_{\Gamma} (\mathbf{F} - \bar{\mathbf{F}}) : \delta \bar{\mathbf{P}} h dS = 0, \quad (10d)$$

$$\int_{\Gamma} (\bar{J} - \bar{J}^*) \delta \bar{p}^* h dS = 0, \quad (10e)$$

where  $\tilde{\mathbf{F}} = \left( \frac{\bar{J}^*}{\bar{J}} \right)^{1/3} \bar{\mathbf{F}}$  and  $\tilde{\mathbf{P}} = \frac{\partial A}{\partial \tilde{\mathbf{F}}}$ . After simplifying, the discrete nodal forces are given by

$$\mathbf{R}_a^{\pm} = \int_{\Gamma} \left( \frac{\bar{J}^*}{\bar{J}} \right)^{1/3} \left( \tilde{\mathbf{P}} - \frac{1}{3} \text{tr}(\tilde{\mathbf{P}} \tilde{\mathbf{F}}^T) \tilde{\mathbf{F}}^{-T} + \bar{J} \bar{p}^* \tilde{\mathbf{F}}^{-T} \right) : \left( \frac{1}{2} \frac{\partial \bar{\mathbf{B}}_a^{\parallel}}{\partial \tilde{\mathbf{x}}_a} \pm \bar{\mathbf{B}}_a^{\perp} \right) h dS, \quad (11)$$

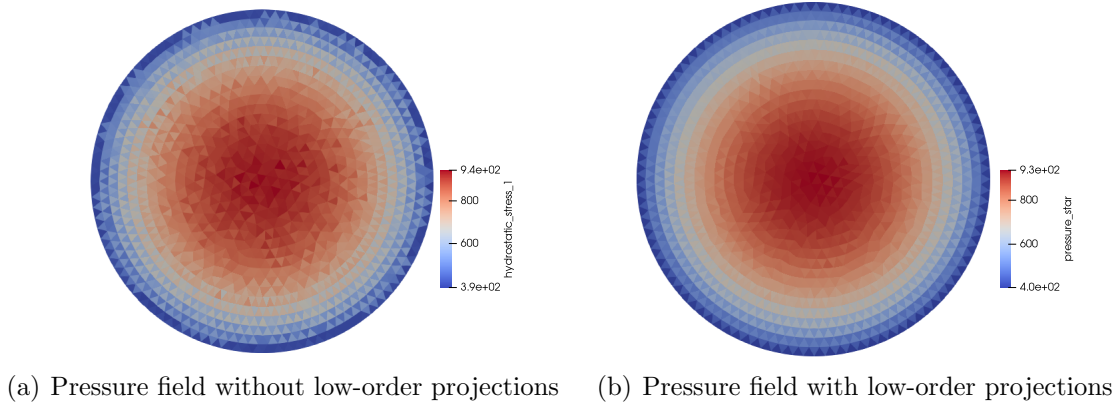


**Figure 5.** Contour plots of the pressure field for elements without lower-order projections and contours of the pressure using lower-order projections.

where  $\bar{\mathcal{B}}_a^{\parallel}$  and  $\bar{\mathcal{B}}_a^{\perp}$  are the projected gradient operators. In Fig. 5, we show the effects of using the lower-order projection for a relatively small deformation. The plots show that the pressure (hydrostatic stress) fields are much smoother when using the lower-order projections. However, the instabilities in the field remain and will become more pronounced as the deformation increases. Using lower-order projections are insufficient to eliminate the volumetric locking and pressure instabilities in the localization element [7].

Similar to the composite tetrahedron [2], when a lower-order projection of the pressure is used on the localization element, additional spurious zero-energy modes appear in the element stiffness matrix of a single element. A stabilization term is added in to the functional

$$\Pi^{\dagger}[\varphi, \bar{\mathbf{F}}, \bar{\mathbf{P}}, \bar{p}^*, \bar{J}^*] := \Pi^{\star}[\varphi, \bar{\mathbf{F}}, \bar{\mathbf{P}}, \bar{p}^*, \bar{J}^*] + \int_{\Gamma} K\left(\frac{\bar{J}^*}{\bar{J}}\right) h dS, \quad (12)$$

where  $K(\cdot)$  is a non-negative convex function satisfying  $K(1) = 0$ . The function  $K$  is chosen so that it penalizes the functional whenever  $\bar{J}^*$  differs from  $\bar{J}$ ; however, when  $\bar{J}^* = \bar{J}$  (elementwise constant) the stabilization contribution vanishes and the element satisfies any linear patch test. Details of the implementation and choice of stabilization function are found in [2].

### Hyperelastic-type stabilization

In the previous section, we utilized the stabilization developed in [2]; however, we found that this approach was not sufficient to eliminate all the zero-energy modes of the composite localization element. In particular, by examining a linear eigenvalue analysis over a single element, we found that the 12-noded localization element has 14 spurious zero-energy modes. After applying the stabilization in (12), there are still 12 spurious modes remaining. Upon assembly with other elements, the global stiffness matrix no longer has zero-energy modes; however, 3 low-energy modes remain. These low-energy modes are excited by certain boundary conditions and lead to nonphysical deformations.

We now consider an alternative approach, given in [8] for the mean-strain hexahedral element and in [9, 10] for the virtual element method. For simplicity, we show the construction of a stabilization for (6); however, for the examples we apply the procedure to (9). We start with a standard energy potential  $\int_{\Gamma} A(\mathbf{F}, \mathbf{Z}) h dS$  and formally write

$$\int_{\Gamma} A(\mathbf{F}, \mathbf{Z}) h dS = \int_{\Gamma} A(\bar{\mathbf{F}}, \mathbf{Z}) h dS + \int_{\Gamma} A(\mathbf{F}, \mathbf{Z}) h dS - \int_{\Gamma} A(\bar{\mathbf{F}}, \mathbf{Z}) h dS. \quad (13)$$

The first term controls the kinematics and the consistency, while the remaining terms give a measure of the stability or error. To control the stability, we only need to approximate the second and third terms:

$$\int_{\Gamma} A(\mathbf{F}, \mathbf{Z}) h dS \approx \int_{\Gamma} A(\bar{\mathbf{F}}, \mathbf{Z}) h dS + \int_{\Gamma} \hat{A}(\mathbf{F}, \mathbf{Z}) h dS - \int_{\Gamma} \hat{A}(\bar{\mathbf{F}}, \mathbf{Z}) h dS, \quad (14)$$

where  $\hat{A}(\cdot, \cdot)$  is the Helmholtz free-energy density of a secondary stabilization material. The choice of  $\hat{A}(\cdot, \cdot)$  is unspecified; however, it should be chosen to be representative of the original material. For our tests, we use a J2-plasticity model for the primary material and a scaled hyperelastic neo-Hookean model for the stabilization material. One concern with using a hyperelastic stabilization material for plasticity problems is that the hyperelastic energy will dominate the energy and stiffen the solution. We expect that using the same material model with differing properties will result in more accurate and stable solutions. Further treatment of the plasticity case is found in [10].

This now motivates the definition of a modified energy functional:

$$\hat{\Pi}[\varphi, \bar{\mathbf{F}}, \bar{\mathbf{P}}] := \int_{\Gamma} A(\bar{\mathbf{F}}, \mathbf{Z}) h dS + \int_{\Gamma} \hat{A}(\mathbf{F}, \mathbf{Z}) h dS - \int_{\Gamma} \hat{A}(\bar{\mathbf{F}}, \mathbf{Z}) h dS + \int_{\Gamma} \bar{\mathbf{P}} : (\mathbf{F} - \bar{\mathbf{F}}) h dS. \quad (15)$$

The terms using  $\bar{\mathbf{F}}$  can be computed with the same approach from the previous section; however, the term involving  $\mathbf{F}$  will need to be computed over subtriangles. That is, for each localization element  $\Gamma_E$  and any function  $f$  we have

$$\int_{\Gamma_E} f(\mathbf{F}) h dS = \sum_{S=0}^3 \int_{\Gamma_E^S} f(\mathbf{F}) h dS,$$

where  $\Gamma_E^S$  ( $S = 0, 1, 2, 3$ ) are the associated subtriangles of an element. On each subtriangle, we apply a Gaussian quadrature scheme to compute the integrals. By solving an element eigenvalue problem, we find that using a 1-point integration gives in an element stiffness matrix with 9 spurious modes, while using a 3-point integration results in only 3. Therefore, we focus on a 3-point quadrature rule in our tests.

In Fig. 6, we plot the deformation and pressure field of a layer of localization elements. We find that without stabilization, the mid-edge nodes around the boundary move upwards, similar to the hourglass modes in underintegrated elements (see Fig. 6(a)). In Fig. 6(c), we show the deformation when using the stabilization. We find that the stabilization scheme

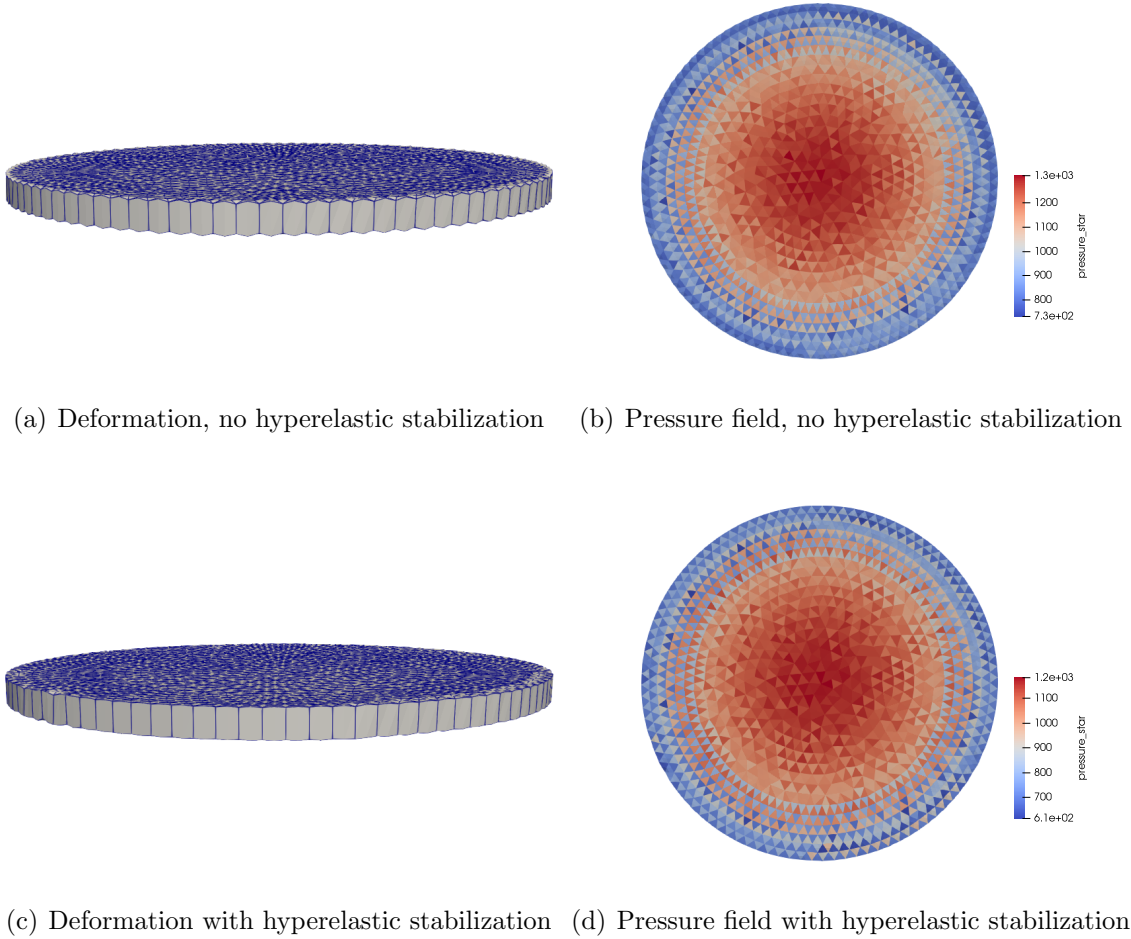


**Figure 6.** Contour plots comparing the deformation and the pressure field for the standard stabilization and additional hyperelastic stabilization.

reduces the spurious motion of the midedge nodes; however, there are signs of element buckling instabilities (over stiffness). The pressure field remains oscillatory in both cases, which suggests that the pressure instabilities are independent of the displacement (inf-sup instability).

In the present approach, we apply the stabilization directly to a multi-field functional. After taking the variation of this functional, stabilization terms will be directly embedded in the associated stress. Further investigations of this stabilization attempt applied to (9) reveal that the pressure is directly influenced by the choice of stabilization parameters and will converge to an incorrect pressure field. However, in the original formulation given in [8, 9], the multi-field functional is first written as a single-field displacement based functional by statically condensing all of the additional fields. The stabilization technique is then applied to the single-field functional and the corresponding stress remains unaffected by the choice

of stabilization. Initial studies show that this original approach is difficult to apply to the five-field functional (9); however, we give an alternative stabilization in the next section.

### Alternate Stabilization

For the five-field formulation (9), directly adding in a stabilization to the functional results in many mixed terms in the definition of the projected quantities. This adds complexity to the formulation and implementation. Instead, we introduce a modified stabilization scheme by applying the stabilization to the weak equilibrium equations given by (10a). Motivated by the hyperelastic-type stabilization (14), we add and subtract stress terms derived from a Helmholtz free-energy density  $\hat{A}(\cdot, \cdot)$ :

$$\begin{aligned} \int_{\Gamma} (\bar{\mathbf{P}} : \text{Grad}(\delta\boldsymbol{\varphi})) h dS &\approx \int_{\Gamma} (\bar{\mathbf{P}} : \text{Grad}(\delta\boldsymbol{\varphi})) h dS \\ &+ \int_{\Gamma} \left( \frac{\partial \hat{A}}{\partial \mathbf{F}} : \text{Grad}(\delta\boldsymbol{\varphi}) \right) h dS - \int_{\Gamma} \left( \frac{\partial \hat{A}}{\partial \bar{\mathbf{F}}} : \text{Grad}(\delta\boldsymbol{\varphi}) \right) h dS. \end{aligned} \quad (16)$$

Then we define the stabilized weak form as

$$\int_{\Gamma} \bar{\mathbf{P}} : \delta \bar{\mathbf{F}} h dS + \int_{\Gamma} \left( \frac{\partial \hat{A}}{\partial \mathbf{F}} : \delta \mathbf{F} \right) h dS - \int_{\Gamma} \left( \frac{\partial \hat{A}}{\partial \bar{\mathbf{F}}} : \delta \bar{\mathbf{F}} \right) h dS = 0, \quad (17)$$

where  $\int_{\Gamma} \bar{\mathbf{P}} : \delta \bar{\mathbf{F}} h dS$  is given by the orthogonality condition in (10b). After simplifying, the nodal forces are given by

$$\begin{aligned} \mathbf{R}_a^{\pm} &= \int_{\Gamma} \left( \frac{\bar{J}^{\star}}{\bar{J}} \right)^{1/3} \left( \bar{\mathbf{P}} - \frac{1}{3} \text{tr}(\bar{\mathbf{P}} \bar{\mathbf{F}}^T) \bar{\mathbf{F}}^{-T} + \bar{J} \bar{p}^{\star} \bar{\mathbf{F}}^{-T} \right) : \left( \frac{1}{2} \frac{\partial \bar{\mathbf{B}}_a^{\parallel}}{\partial \bar{\mathbf{x}}_a} \pm \bar{\mathbf{B}}_a^{\perp} \right) h dS \\ &+ \int_{\Gamma} \frac{\partial \hat{A}}{\partial \mathbf{F}} : \left( \frac{1}{2} \frac{\partial \mathbf{B}_a^{\parallel}}{\partial \tilde{\mathbf{x}}_a} \pm \mathbf{B}_a^{\perp} \right) h dS - \int_{\Gamma} \frac{\partial \hat{A}}{\partial \bar{\mathbf{F}}} : \left( \frac{1}{2} \frac{\partial \bar{\mathbf{B}}_a^{\parallel}}{\partial \bar{\mathbf{x}}_a} \pm \bar{\mathbf{B}}_a^{\perp} \right) h dS. \end{aligned} \quad (18)$$

For simplicity, we choose  $\hat{A}$  to be the strain energy density derived from a scaled neo-Hookean material. We can either use the same elastic material properties  $\mu$  and  $\kappa$  from the bulk material

$$\hat{A} = \beta \left[ \frac{\kappa}{2} \left( \frac{1}{2} (J^2 - 1) - \ln J \right) + \frac{\mu}{2} \left( \text{tr}(\bar{\mathbf{C}}) - 3 \right) \right], \quad (19a)$$

or use modified material properties  $\hat{\mu}$  and  $\hat{\kappa}$

$$\hat{A} = \beta \left[ \frac{\hat{\kappa}}{2} \left( \frac{1}{2} (J^2 - 1) - \ln J \right) + \frac{\hat{\mu}}{2} \left( \text{tr}(\bar{\mathbf{C}}) - 3 \right) \right], \quad (19b)$$

where  $\bar{\mathbf{C}}$  is the isochoric part of the Cauchy-Green tensor. Careful selection of the modified material properties is needed to ensure that the stabilization term does not overly stiffen the results. Performing a linear eigenvalue analysis, we find that using a 1-point quadrature on each subtriangle gives 3 spurious zero-energy modes and 8 relatively low energy modes, while using a 3-point scheme retains the 3 spurious modes but does not have the lower energy modes. Therefore, we again use a 3-point integration for the following examples.



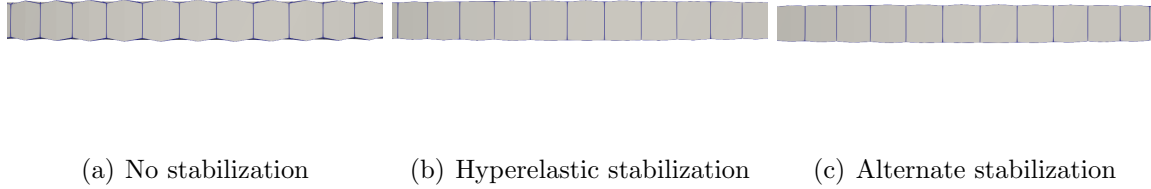


**Figure 7.** Side view of deformation for localization elements with fixed  $h = 0.1$  mm while utilizing different stabilization methods.

We first compare the performance of the two stabilization techniques. In Fig. 7, we examine the deformation of localization elements with and without the use of stabilization. We find that both the stabilization methods reduce the appearance of the hourglass-type deformation. Further testing showed that the two approaches give nearly identical deformations when using the same stabilization material.

In Fig. 8, contour plots comparing the pressure fields of the nonstabilized to the stabilized elements are given. The localization element is assumed to have a length scale  $h = 1$  mm. The plots show that the nonstabilized element suffer from large buckling and dimpling in the deformation. The two stabilized methods eliminated these instabilities for the shown time step. However, we note that magnitude of the pressure of the first stabilization is much lower than the other two (see Fig. 8(b) and 8(c)). This mismatch is because of an additional mixed term found in the variational pressure relation of the first scheme.

One problem with using a stabilization is the need to choose a suitable scale factor to minimize the effects of hourglass-type modes while not overconstraining and overstiffening the physical deformation modes. In Fig. 9, we show the deformation of a collection of localization elements when using the stabilization material (19a) with the scale factors  $\beta = 0.05, 0.1, 0.2$ . For  $\beta = 0.05$ , the nonphysical modes are reduced but still visible on both

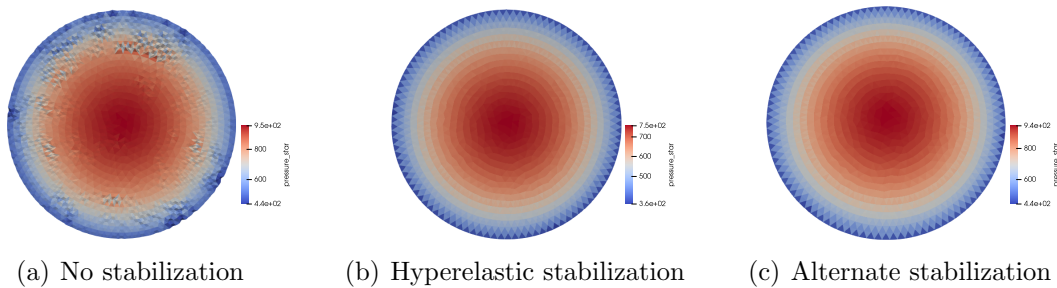


**Figure 8.** Contour plots of the pressure for localization elements with fixed  $h = 1$  mm while utilizing different stabilization methods.



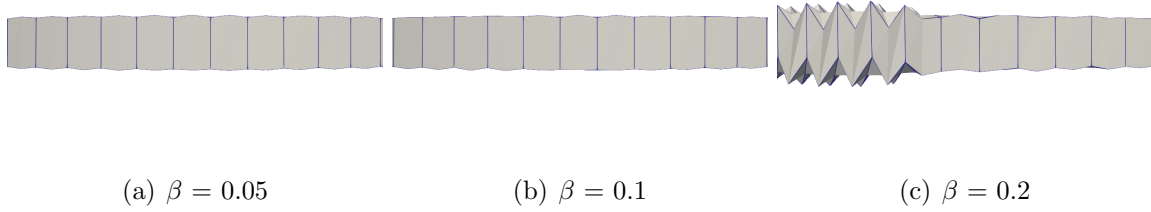


**Figure 9.** Side view of a larger deformation for localization elements with fixed  $h = 0.1$  mm and different stabilization coefficient  $\beta$  for (19a).

top and bottom surfaces, while with  $\beta = 0.1$  the modes seem to flip between the two surfaces. Once  $\beta = 0.2$ , some of the elements buckle and completely fail (see Fig. 9(c)). This shows that overstiffening the element with a large stabilization parameter can lead to severe element instabilities. These instabilities closely resemble the material hourglass modes of the enhanced element formulations explored in [11]. In [10], it is suggested that  $\beta$  should decrease as the material hardens during plastic deformation.

### Localization elements in general

In the previous sections, we found that adding a stabilization term can improve the deformation fields in some cases but can also introduce other complications and doesn't seem to improve the pressure fields. Therefore, in this section, we study different examples using the five-field formulation (9) without any stabilization.

We first examine the effects of different  $h$  values on the pressure fields of the localization element. In Fig. 10, the contour plots of the pressure field for four values of  $h$  are given. The plots show that for a fixed mesh, the pressure fields begin to lock and oscillate as  $h \rightarrow 0$ . For bigger  $h$ , the fields appear smoother; however, we note that Fig. 10(a) shows buckling instabilities in the deformation. This suggests that choosing  $h$  too small will result in locking of the pressure, but having  $h$  too large leads to nonphysical kinematics. We further study these effects in following examples.

We study the effects of  $h$  on the kinematics in the normal direction. We plot the deformed state of the localization element for the notched tension problem using different values of  $h$  in Fig. 11. We find that increasing the length scale  $h$  softens the element and allows for it expand in the out-of-plane direction. Taking  $h$  smaller will restrict the motion in the normal direction and as  $h \rightarrow 0$ , the elements can only deform in-plane.

We next consider the effects of  $h$  on the tangential kinematics of an object. We solve the problem of a compressible neo-Hookean block ( $\nu = 0.0$ ) subjected to a displacement on the top and bottom edge. The block is modeled as two layers of tetrahedral elements connected by a layer of localization elements. In Fig. 12, plots of the deformed block are shown for a fully

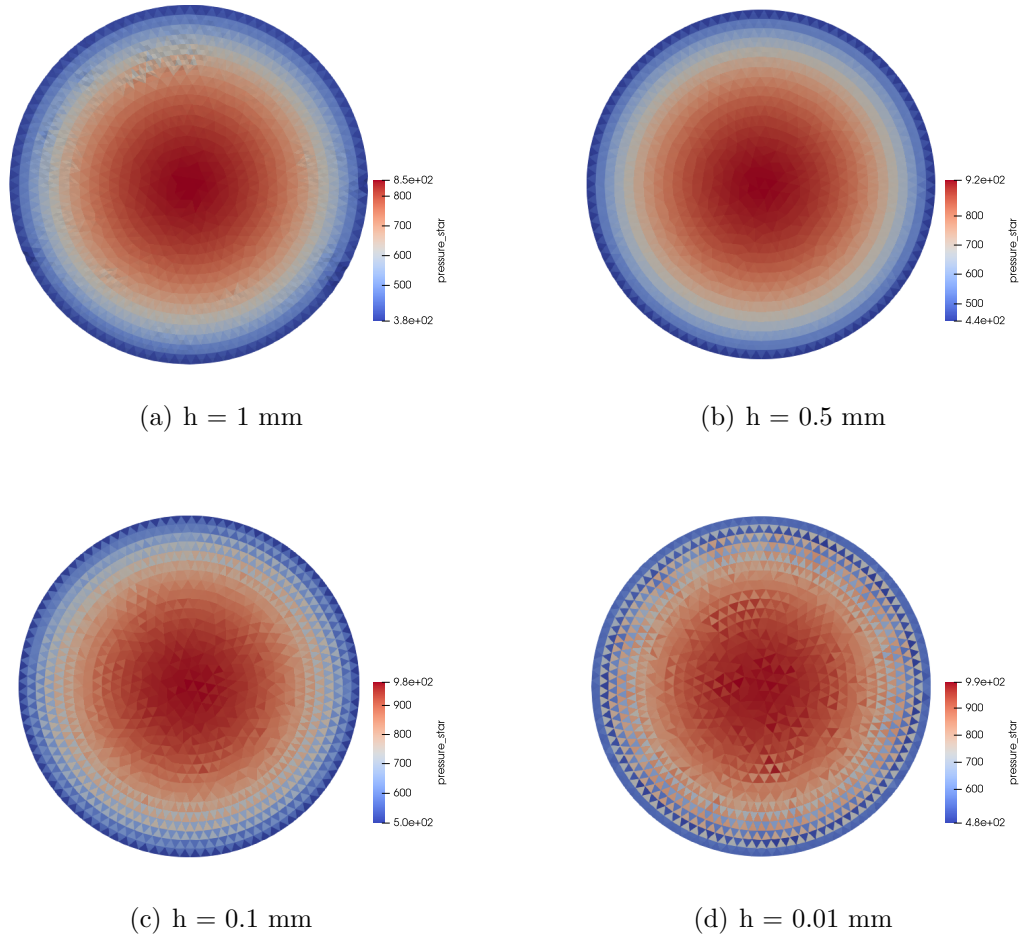


**Figure 10.** Contour plots of the projected pressure  $\bar{p}^*$  for different  $h$  on a fixed mesh.

tetrahedral mesh and meshes including the localization elements with different  $h$ . We find that for  $h = 1 \text{ mm}$ , the two tetrahedral layers slide past each other without any interactions. As  $h \rightarrow 0$ , the deformation with localization elements converges to the deformation with only tetrahedral elements. This implies that for meshes using localization elements, the length scale  $h$  should initially be small to not interfere with the deformation of the bulk elements.

We now test the effects of changing the mesh size while fixing a value of  $h$ . Contour plots of the projected pressure  $\bar{p}^*$  for a fixed length scale  $h = 0.1 \text{ mm}$  with varying mesh refinements are shown in Fig. 13. The plots seem to indicate that for a given  $h$ , refinement will smooth out the pressure fields. In Fig. 14(a) a magnified plot shows that the oscillations do appear but are greatly reduced for the refined mesh. However, Fig. 14(b) shows additional deformation of the refined mesh results in large oscillations in pressure. This suggests that while refinement can temporarily improve the pressure fields for a fixed deformation state, instabilities reappear upon further deformation.

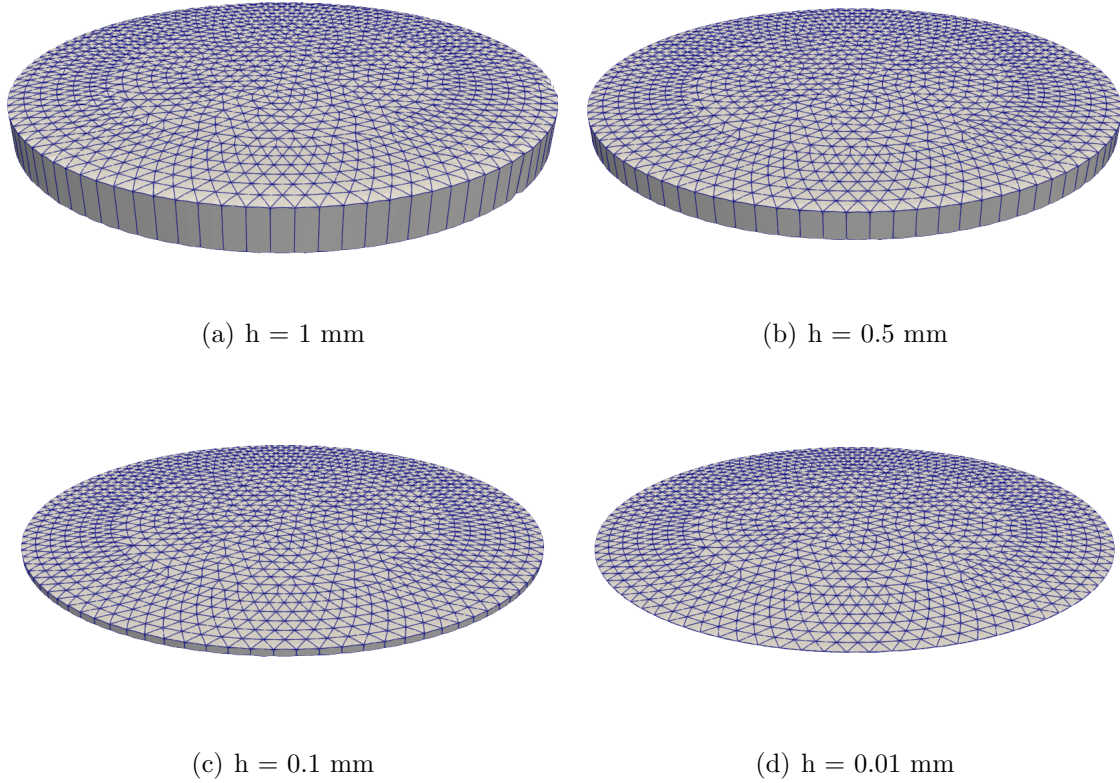


**Figure 11.** Comparison of the normal deformation of a plate for different  $h$ .

In earlier studies, it was shown that a hexahedral localization element with a mean dilatation formulation provided smoother pressure fields and more robust behavior at the cost of more difficult meshing. As a comparison, we rerun some tests on meshes with similar sized hexahedral localization elements. In Fig. 15, we plot the contours of the hydrostatic stress on a fixed mesh with varying length scales  $h$ .

We also plot the contours plots of the hydrostatic stress on meshes of different refinements in Fig. 16 and magnified plots in Fig. 17. The plots show that, while the hexahedral elements have smoother stresses in some cases, similar instabilities are present when  $h \rightarrow 0$  or in large deformations.

**Remark 1** *We note that while both the composite wedge elements and the hexahedral localization elements have instabilities for  $h \rightarrow 0$  or for large deformations, their appearance in the contour plots are different. For the composite wedge element, the pressure instabilities appear as oscillations between neighboring elements, known as the checkerboard instability. While in the hexahedral elements, the hydrostatic stress oscillates between multiple elements and creates the appearance of a smoother solution (compare Fig. 10(d) and 15(d)).*

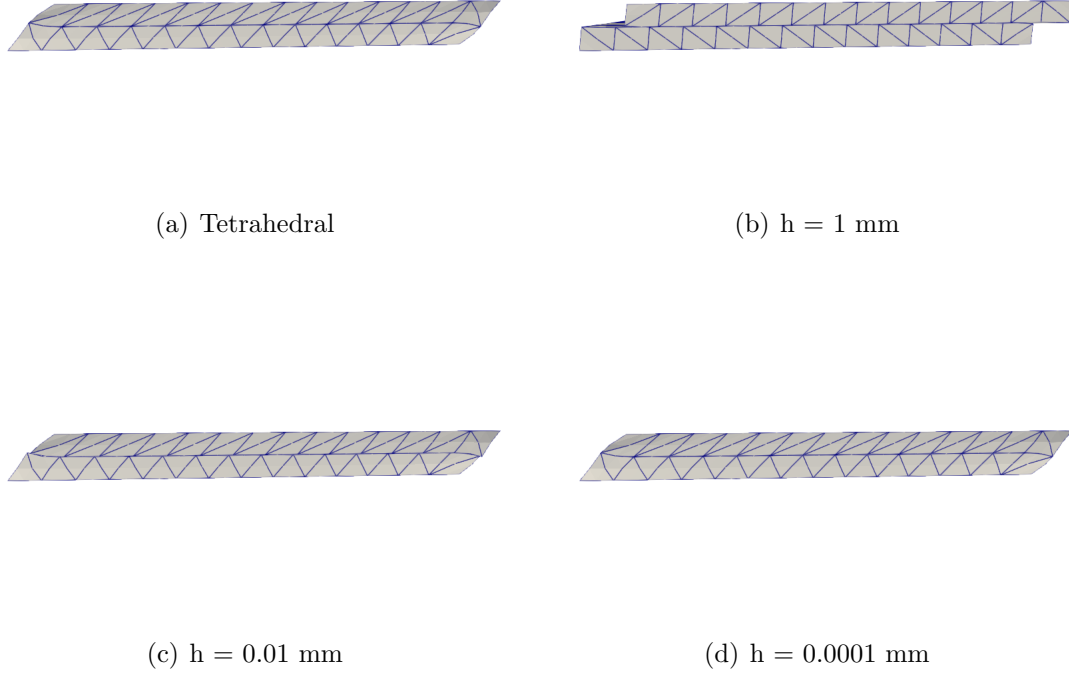


**Figure 12.** Plots of the tangential deformation of a plate for different  $h$ .

In the previous examples, we looked at the pressure fields of a material in the plastic (nearly-incompressible) regime and found that the solution is very sensitive to the length scale  $h$ . It is expected that for compressible materials, there are no pressure instabilities and so no sensitivity to  $h$ . We now consider a simplified problem of a circular plate with two layers of tetrahedral elements connected by a layer of localization elements. The material is assumed

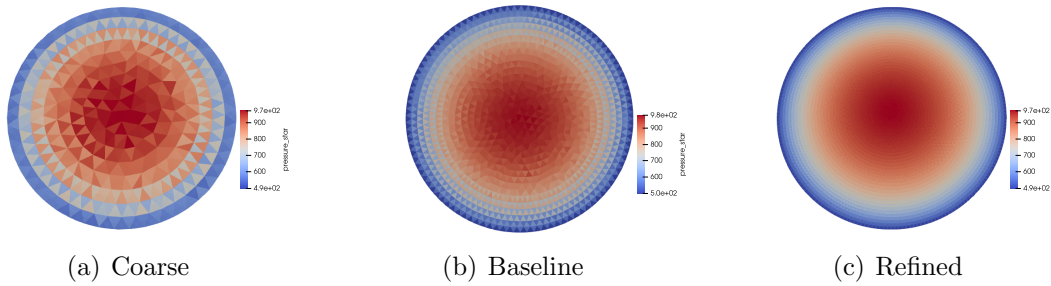


**Figure 13.** Contour plots of the projected pressure  $\bar{p}^*$  for composite localization elements with fixed  $h = 0.1$  mm and varying mesh refinement.

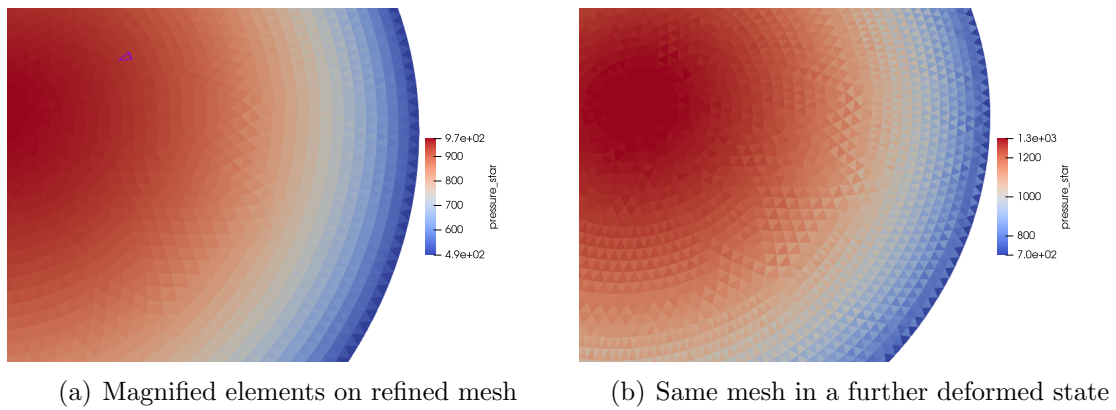


**Figure 14.** Contour plot showing a magnification of representative elements in the refined mesh and another under further deformation.

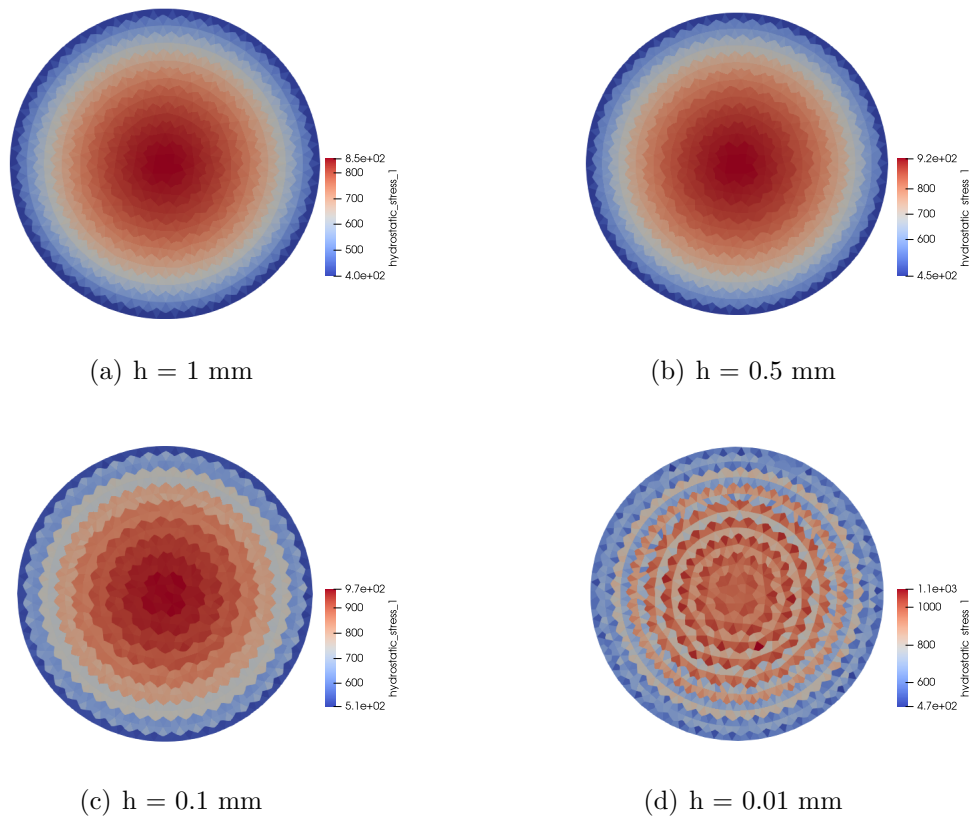


**Figure 15.** Contour plots of the pressure for different  $h$  on a fixed hexahedral mesh.



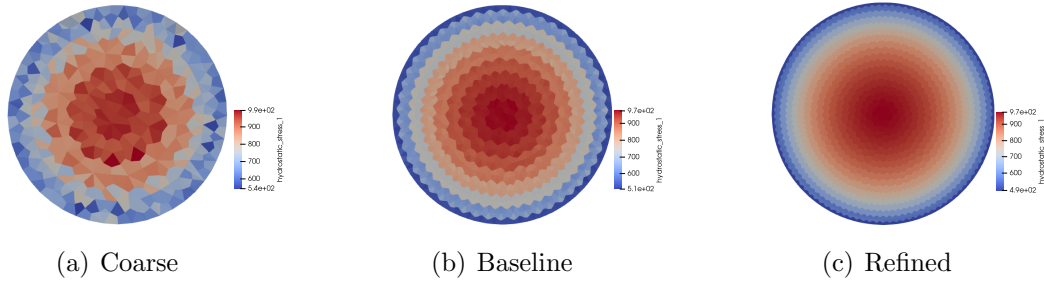


**Figure 16.** Contour plots of the hydrostatic stress for hexahedral localization elements with fixed  $h = 0.1$  mm and varying mesh refinement.

to follow a compressible neo-Hookean model with Poisson's ratio  $\nu = 0.4$ . A quadratic displacement field is applied to the top and bottom surfaces. In Fig. 18, we present contour plots of  $\bar{p}^*$  for  $h = 0.1, 0.01$ , and  $0.0001$  mm. The plots show that for a compressible material, the pressure fields are not sensitive to the length scale parameter going to 0 ( $h \rightarrow 0$ ), but displacement instabilities appear for sufficiently large  $h$ . This suggests that taking  $h$  small adds constraints to the deformation and leads to volumetric locking for nearly-incompressible materials, while taking  $h$  large excites displacement modes (nonphysical zero-energy modes or material instability modes) independent of the compressibility of the material.

From all these examples, we suspect that connecting the composite wedge localization element to bulk elements overconstrains the motion and results in volumetric locking (failure of the inf-sup condition) when the material becomes incompressible. From (5), the deformation gradient has all the components representing in-plane and transverse motion; however, it does not have any of the components corresponding to out-of-plane shear. The missing shear components restrict how the localization elements can deform in shear, while the bulk elements do not have this restriction. This results in the localization element having fewer

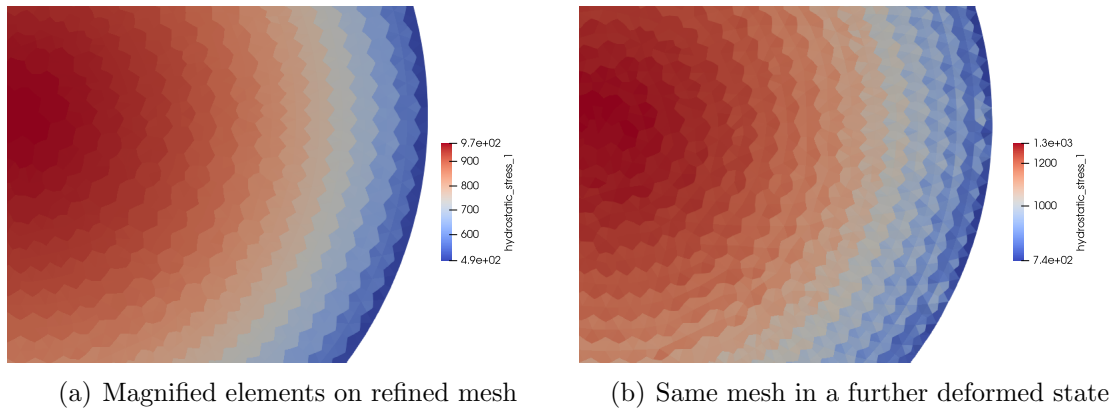


**Figure 17.** Contour plot showing a magnification of representative elements in the refined hexahedral mesh and another under further deformation.

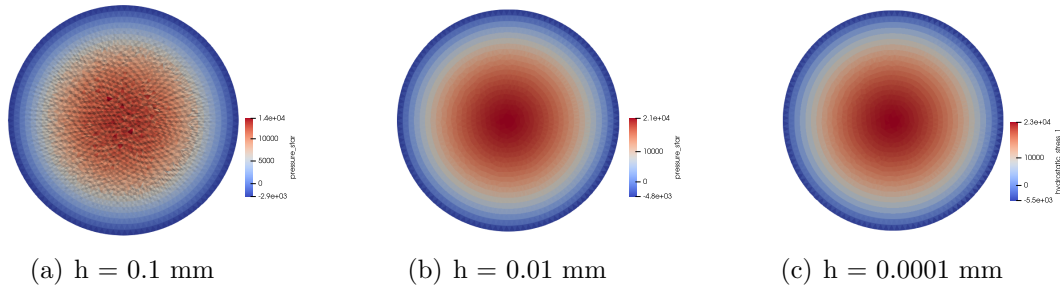


**Figure 18.** Contour plots of the projected pressure  $\bar{p}^*$  for a compressible neo-Hookean material with different values of  $h$ .

degrees of freedom that can be used to satisfy the incompressibility condition and produce the correct deformation. Thus, under sufficient incompressibility and non-uniform deformation, the two types of elements can no longer consistently deform in a way that keeps the volume constant. By starting with a larger value of  $h$ , the localization elements have more freedom to move in both the normal and tangential directions (see Fig. 11 and 12) which allows for easier satisfaction of the incompressibility condition; however, this comes at the cost of displacement instabilities and nonphysical motion. Similar problems occur for the fully-integrated isoparametric hexahedral element which does not have sufficient deformation modes to enforce near-incompressibility or bending. One solution is using an enhanced assumed strain approach [12, 13], where additional incompatible strain modes are selectively added to soften the element and reduces volumetric and shear locking. However, in some cases it was shown that having these incompatible modes between elements introduced non-physical instabilities in large deformation [11, 14, 15]. Another possibility is to use a mixed method with an independent pressure. But it was shown that these elements do not always satisfy an inf-sup (LBB) stability condition and the resulting elements can exhibit the checkerboard pressure mode [16].

**Remark 2** *For this work, we fixed the length scale  $h$  to be constant for all elements; however, in the original localization element [1], the length scale evolves according to a variational principle. It was shown that  $h$  will change over time and depends on the current deformation state. Using the variational principle adds complexity and restricts the element to certain problems. Our initial attempts to replicate a nonconstant  $h$  by applying an update for each timestep resulted in solver convergence issues.*

## Conclusion

In this memo, we studied an extension of the localization element that is compatible with the 10-node composite tetrahedron. The resulting element is a 12-noded wedge with four composite subtriangles. On each subtriangle, the deformation map is assumed to be piecewise linear and continuous across elements. The deformation gradient and the First Piola-Kirchoff stress are constructed to be linear on the parent element but discontinuous between

elements. To alleviate some symptoms of volumetric locking, a five-field functional using lower-order constant projections for the pressure and Jacobian was used. However, even with the lower-order projections, we found that this element continued to suffer from pressure checkerboarding and nonphysical hourglass-type deformations. While investigating the eigenvalues of the linearized element stiffness matrix, we found that the element produced 14 spurious zero-energy modes. Using an initial stabilization technique following [2] reduced the number of spurious modes to 12. To further reduce the number of spurious modes, we introduced two energy-based stabilization schemes following [8, 9]. By using these schemes and a 3-point Gauss quadrature on each subtriangle, only three excess zero-energy modes remained. This reduced the severity of hourglass-type deformation modes; however, the pressure checkerboarding and instabilities were unaffected. Since the use of a stabilization did not seem to influence the pressure, we investigated the length scale  $h$  inherent to the localization element. We first examined the case where the mesh is fixed and  $h$  is varied. We found that decreasing  $h$  leads to highly oscillatory pressure fields, while increasing  $h$  introduces instabilities in the deformation. In addition, using a large value of  $h$  resulted in overly large deformations in the normal and tangential directions. Next, we tested the case with a fixed  $h$  and varying the mesh density. The results showed that mesh refinement does appear to smooth out the pressure fields at a given deformation state; however, the instabilities reappear after further loading. These problems are shared between both the composite wedge and the hexahedral localization elements, so we suspect that the missing shear components of the localization element, combined with near-incompressibility results in an overstiff response (locking) and pressure instabilities. Another potential issue is that the length scale  $h$  cannot be a fixed value and should evolve under deformation. In the original formulation, the factor  $h$  was chosen at each step to enforce an equilibrium condition, but by fixing  $h$  the resulting solutions may not be physical.

In this work, we found that by choosing suitable stabilization parameters, the buckling and nonphysical deformations can be reduced; however, stabilizing the deformation is not sufficient to prevent volumetric locking or satisfy an inf-sup stability condition. Therefore, other techniques such as using inf-sup stable mixed elements [16], higher order methods and enhanced strain approaches [12] should be investigated. Other common methods used to smooth out pressure checkerboarding in fluid flow problems is to add in a pressure jump stabilization [17] or a residual based stabilization [18]. These terms penalize the spurious pressure oscillations and lead to smoother solutions but require specialized implementation.

## Acknowledgements

Sandia National Laboratories is a multitechnology laboratory managed and operated by the National Technology & Engineering Solutions of Sandia, LLC, a wholly owned subsidiary of Honeywell International Inc., for the U.S. Department of Energy's National Nuclear Security Administration under contract DE-NA0003525.



## References

- [1] Q. Yang, A. Mota, and M. Ortiz, [Int. J. Num. Meth. Eng. \*\*62\*\*, 1013 \(2005\)](#).
- [2] J. W. Foulk III, J. T. Ostien, B. Talamini, M. R. Tupek, N. K. Crane, A. Mota, and M. G. Veilleux, [Int. J. Num. Meth. Eng. \*\*122\*\*, 3845 \(2021\)](#).
- [3] M. Ortiz and A. Pandolfi, [Int. J. Num. Meth. Eng. \*\*44\*\*, 1267 \(1999\)](#).
- [4] M. R. Buche, M. G. Veilleux, E. B. Wagman, J. M. Emery, A. Mota, and J. W. F. III, [17th U.S. National Congress on Computational Mechanics \(2023\)](#).
- [5] Comp. Solid Mech. & Structural Dyn., [Sandia National Laboratories \(2023\)](#).
- [6] T. D. Kostka, [Sandia National Laboratories \(2013\)](#).
- [7] M. R. Buche, M. G. Veilleux, E. B. Wagman, J. M. Emery, A. Mota, and J. W. F. III, [16th World Congress on Computational Mechanics \(2024\)](#).
- [8] P. Krysl, [Finite Elem. Anal. Des. \*\*108\*\*, 41 \(2016\)](#).
- [9] P. Wriggers, B. D. Reddy, W. Rust, and B. Hudobivnik, [Comput. Mech. \*\*60\*\*, 253 \(2017\)](#).
- [10] P. Wriggers and B. Hudobivnik, [Comput. Meth. Appl. Mech. Eng. \*\*327\*\*, 459 \(2017\)](#).
- [11] S. Bieber, F. Auricchio, A. Reali, and M. Bischoff, [Int. J. Num. Meth. Eng. \*\*124\*\*, 2638 \(2023\)](#).
- [12] J. Simo, F. Armero, and R. Taylor, [Comput. Meth. Appl. Mech. Eng. \*\*110\*\*, 359 \(1993\)](#).
- [13] R. Alves de Sousa, R. Natal Jorge, R. Fontes Valente, and J. César de Sá, [Eng. Computation \*\*20\*\*, 896 \(2003\)](#).
- [14] T. Sussman and K.-J. Bathe, [Comput. Struct. \*\*140\*\*, 14 \(2014\)](#).
- [15] S. Doll, K. Schweizerhof, R. Hauptmann, and C. Freischläger, [Eng. Computation \*\*17\*\*, 874 \(2000\)](#).
- [16] D. Chapelle and K. Bathe, [Comput. Struct. \*\*47\*\*, 537 \(1993\)](#).
- [17] D. Silvester and N. Kechkar, [Comput. Meth. Appl. Mech. Eng. \*\*79\*\*, 71 \(1990\)](#).
- [18] E. Oñate, P. Nadukandi, S. R. Idelsohn, J. García, and C. Felippa, [Int. J. Num. Meth. Fl. \*\*65\*\*, 106 \(2011\)](#).

## Internal Distribution:

Ellen Wagman (1542)  
 Mike Veilleux (1542)  
 John Emery (1556)  
 Stacy Nelson (1558)  
 Jay Foulk (8363)  
 Alejandro Mota (8363)